Constraints on the Neutron Star Mass Distribution and the Equation of State

Emily Ramey[1] and Sergiy Vasylyev[1]

[1] *Department of Astronomy and Astrophysics, University of California, Berkeley, CA 94720, USA*

ABSTRACT

Since Neutron Stars (NS) were first discovered, the distribution of their masses has largely been unknown. Few systems have the required properties for precise mass measurement, leading to a scarcity of mass data in the field. However, recent advancements in relativistic pulsar timing and Doppler spectroscopy have enabled more precise mass measurements. This, in combination with the advent of of gravitational wave astronomy, promises an influx of NS data in the next decade. The goal of this paper is to review current research on the mass distribution of neutron stars and explore the important research problems facing the field today, such as the mass gap between NS and black holes (BH), constraints on the NS Equation of State (EoS), and possible limits on the maximum mass of a Neutron Star. We compare two statistical approaches to determine the mass distribution for different NS types. We find that NS found in different environments favor different EoS models, suggesting that different formation histories lead to different internal structures.

Keywords: neutron stars, mass limit, binaries

1. INTRODUCTION

The first reliable pulsar mass measurement came from PSR B1913+16 in 1975 (Hulse & Taylor 1975). Since then, dozens of measurements have been made with improved precision using relativistic timing and spectroscopy techniques. A particularly surprising result is the gap between 3-5$M_\odot$ in the observed mass distribution of compact objects, shown in Figure 1 (Belczynski et al. 2012). With increased Neutron Star (NS) mass measurements, this apparent region of missing mass has only become more significant. In order to understand this mass gap, it is necessary for both the NS and BH mass distributions to be better constrained, and this review focuses on the former.

Neutron star systems can be classified into 4 main groups: Double Neutron Stars (DNS), Recycled Pulsars (RPs), Bursters, and Slow Pulsars (SPs)(Ozel & Freire 2016). DNS systems consist of a binary pair of NSs that lose their orbital energy to gravitational wave radiation. The NS-NS merger GW170817 detected by the Laser Interferometer Gravitational Wave Observatory (LIGO) and the Virgo interferometer in August 2017, falls into this category (Abbott et al. 2017). RPs are old, primarily radio or x-ray emitting pulsars that have a white dwarf (WD) or main sequence (MS) companion. These pulsars are also referred to as "millisecond pulsars" describing their abnormally high spin rates caused by the accretion of gas from their companions. Through mass transfer mechanisms, these objects have been shown to spin up to as much as 716 Hz (Hessels et al. 2006).
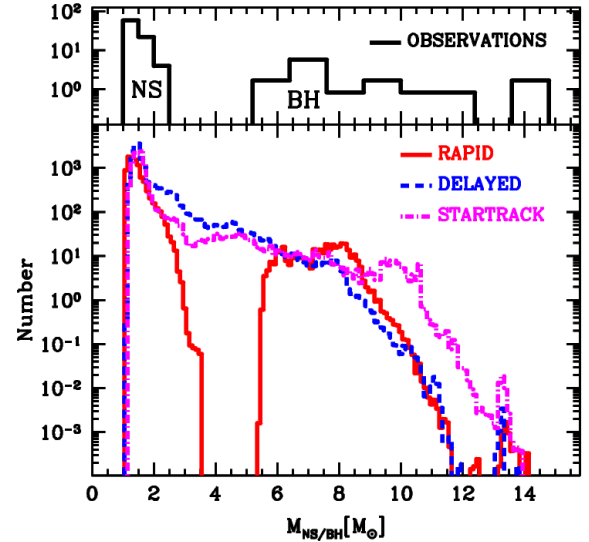

Figure 1. Figure from Belczynski et al. (2012). Top panel: Observational data of compact objects illustrating the mass gap from 3-5$M_\odot$. Bottom Panel: The red line and blue lines are the predicted mass distributions given a rapid and delayed supernova mechanism, respectively. The purple line shows the STARTRACK-modeled mass distribution, which favors a delayed supernova model.

Bursters, or thermonuclear X-ray bursters, are different from RPs in that their emission is primarily driven by thermonuclear processes, not through rotation or accretion. SPs are slow spinning objects that tend to be closely paired with a high mass companion.

Theoretical modeling of the NS Equation of State (EoS) is largely driven by observations, as our current understanding of matter in extreme gravity and density is limited. One of the probes for constraining the EoS is to obtain the maximum mass of a NS, which can be inferred from precise observational measurements of the NS mass distribution (Kalogera & Baym 1996). These constraints can then be used to rule out any EoS which do not match the NS mass limits inferred from observations.

Here, we outline the current progress made in the search for constraints on the NS mass distribution and a comprehensive Neutron Star equation of state (EoS). We use the influx of new pulsar data and the rise of multi-messenger astronomy to infer a NS least upper mass limit, and compare the observationally inferred neutron star structure to the most up to date EoS models.

2. NEUTRON STAR EQUATION OF STATE

The modern approach to calculating an Equation of State (EoS) for neutron star matter involves complex nuclear physics and quantum mechanics. These nuclear models are accurate up to densities in the vicinity of the nuclear matter saturation density $\rho_{sat} = 2.7 \times 10^{14} g/cm^3$, i.e the density at which nuclei begin to physically overlap (Kalogera & Baym 1996). Neutron star central densities are expected to reach several times the saturation density, meaning that these models fail to explain the vast majority of NS structure. Efforts to constrain EoS models for densities exceeding ρ_{sat} have relied on the one-to-one mapping of the observationally inferred mass-radius relation and the EoS (Raithel et al. 2017). Another powerful method of constraining EoS models has been to test the predicted maximum masses with the observed least upper limit on the NS mass. In this paper, we focus on the latter method and show our results in Section 4.1.

Next, we introduce the assumed polytropic form of the NS EoS. A naive approach, assuming the NS consists primarily of non-relativistic, degenerate matter, produces an upper limit of 5.8 $M_\odot$. However, this model fails to explain the observed NS mass distribution (Lattimer & Prakash 2001). We must therefore assume a relativistic, degenerate state of matter to describe the equation of state. Given the compactness of neutron stars, we must also consider the effects of extreme gravity.

Table 1. Equation of State Models

EoS	Composition	$M_{\max}$ [$M_\odot$]	$R_{1.4}$ $[km]^a$
[1]ALF1	$n + p + Q$	1.50	9.90r
[1]ALF2	$n + p + Q$	2.06	13.19
[2]SLy	$n + p$	1.74	11.74
[3]AP2	$n + p$	1.79	10.13
[4]SQM1	Q	1.54	8.86
[4]SQM2	Q	1.74	10.03
[5]H4	$n + p + H$	2.06	13.76
[6]MPA1	$n + p$	2.47	12.47

n = neutrons, p = protons, Q = quarks, H = hyperons. Models are taken from Alford et al. (2005)[1], Douchin & Haensel (2001)[2], Akmal et al. (1998)[3], Prakash et al. (1995)[4], Lackey et al. (2006)[5], Müther et al. (1987)[6].

[a]The NS radius $R_{1.4}$ is evaluated at $M = 1.4 M_\odot$.

2.1. General Relativistic Hydrostatic Equilibrium

We can derive the pressure as a function of the neutron star's radius by integrating the Tolman-Oppenheimer-Volkoff (TOV) equation, which can be interpreted as the relativistic form of the equation for Hydrostatic Equilibrium (HE):

$$\frac{dP}{dr} = -\frac{G}{r^2}\left[\rho(r) + \frac{P(r)}{c^2}\right] \times \frac{m(r) + 4\pi r^3 \frac{P(r)}{c^2}}{1 - 2G\frac{m(r)}{rc^2}} \quad (1)$$

where $m(r)$ is the mass enclosed within a radius, r, and $P(r)$ is the pressure at r inside the star. We assume that the mass continuity equation applies:

$$\frac{dm}{dr} = 4\pi r^2 \rho \quad (2)$$

Note that in the literature, Equations 1 and 2 may also be written in terms of the energy density ϵ, where $\rho = \epsilon/c^2$. We also assume that P(r) follows a polytropic form, giving us a template Equation of State:

$$P(r) = K\rho^\Gamma \quad (3)$$

where Γ is the polytropic index. However, in contrast to the canonical WD polytrope, a neutron star is described more completely by a piece-wise polytrope. In other words, the neutron star is divided into several regions with respect to some reference density, known as the fiducial density, ρ_0 (Raithel et al. 2017). The fiducial density is chosen such that the properties of neutron star matter can only accurately be described for densities lower than this threshold. Depending on the EoS model, this threshold is typically set as a multiple of ρ_{sat}.

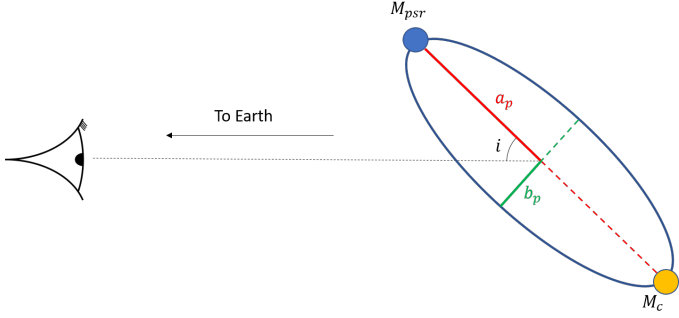In this paper, we focus on a subset of EoS models to demonstrate the ability to constrain these models from

Figure 2. Geometry of a pulsar binary system. M_{psr} and M_c are the pulsar and companion mass, respectively. The semi-major and semi-minor axes are labeled a_p and b_p, respectively. The inclination angle i is measured from the line of sight to observer.

observable NS properties. The various models we use assume piece-wise functional forms for the EoS and are chosen to cover a wide parameter space. Model parameters are listed in Table 1.

MAXIMUM NEUTRON STAR MASS

In general, the maximum mass of a Neutron Star is dictated by the stiffness of the EoS, or how steeply the pressure scales with density. A soft equation of state (more compressible matter) will yield a lower M_{max} than a stiff equation of state. In this paper, we assume that the threshold for what is considered stiff is $\Gamma \geq 5/3$ (Lattimer & Prakash 2001). Rhoades & Ruffini (1974) first showed that a NS reaches its maximum mass when the speed of sound through the nuclear matter approaches the speed of light ($dP/d\rho \approx c$), which occurs at different points for different EoS models. We include the theoretical maximum NS masses for the different EoS models in Table 1.

3. MASS MEASUREMENT TECHNIQUES

In order to confirm or rule out the theoretical EoS models, observations of the NS mass distribution must be made and constraints on the maximum NS mass must be inferred. Most known NS masses have been discovered through two primary techniques: a combination of relativistic pulsar timing and post-Keplerian physics, and Doppler spectroscopy using strong emission lines. Only recently have we been able to estimate the component masses in a binary NS system without relying solely on those two methods, starting with the discovery of gravitational waves from the merger GW170817 by the Laser Interferometer Gravitational-Wave Observatory (LIGO) (Abbott et al. 2017).

3.1. *Relativistic Pulsar Timing: Post-Keplerian Parameters*

From radio observations of pulsars, one can obtain 5 keplerian orbital parameters: the binary's orbital Period, P_b, the line-of-sight projected semi-major axis, $x_{PSR} = a_p \sin i$ (measured in light-seconds), the eccentricity, e, the longitude, ω_0, and the time of periastron (closest approach to companion star), T_0. When gravitational effects are weak, the pulsar mass can be related to:

$$f = \frac{(M_c \sin i)^3}{M^2} = \left(\frac{2\pi}{P_b}\right)^2 x_{PSR}^3 T_\odot^{-1} \quad (4)$$

where M_c and M are the the companion mass and the total mass of the system, respectively. The pulsar mass is then $M_{PSR} = M - M_c$. Here, $T_\odot = GM_\odot/c^3$.

In order to resolve the pulsar mass, one must obtain a constraint on the inclination, i, of the orbit and on the companion mass (See Figure 2). If the semi major axis of the companion can be measured and the companion is a white dwarf (WD) or main sequence star, then another parameter can be used to break the degeneracy in the equation above, defined as the mass ratio, q:

$$q \equiv \frac{M_{PSR}}{M_c} = \frac{x_{PSR}}{x_c} \quad (5)$$

When gravitational dilation effects are taken into account, we must use the five post-Keplerian (PK) parameters defined in Section 3b) of Taylor (1993):

1. The rate of advance of the periastron, $\dot{\omega}$

2. The time delay due to gravitational-redshift effects known as the the Einstein delay, γ

3. The change in the orbital period, $\dot{P_b}$

4. The range of the Shapiro delay, r

5. The quantity related to the shape of the Shapiro delay, s.

The Shapiro delay is the delay in the time of arrival of information from a source due to light taking paths of different length through curved space-time around the source. This effect is amplified when viewing a binary system edge on ($i = 0$).

It is a difficult task to measure these parameters. However, only two are needed to accurately measure the pulsar mass, M_{PSR}, and the companion mass, M_c. Examples of this pairwise requirement include J0348+0432 (q, M_{WD}), J0437-4715 (r, s), J1906+0746 ($\dot{\omega}$, γ), J0751+1807 ($\dot{P_b}$, s) (Antoniadis et al. 2013; Reardon et al. 2016; Leeuwen et al. 2015; Desvignes et al. 2016).

DNS systems that have two or more PK parameters observed produce very tight constraints on the mass measurement (Ozel et al 2012). Therefore, we expect a
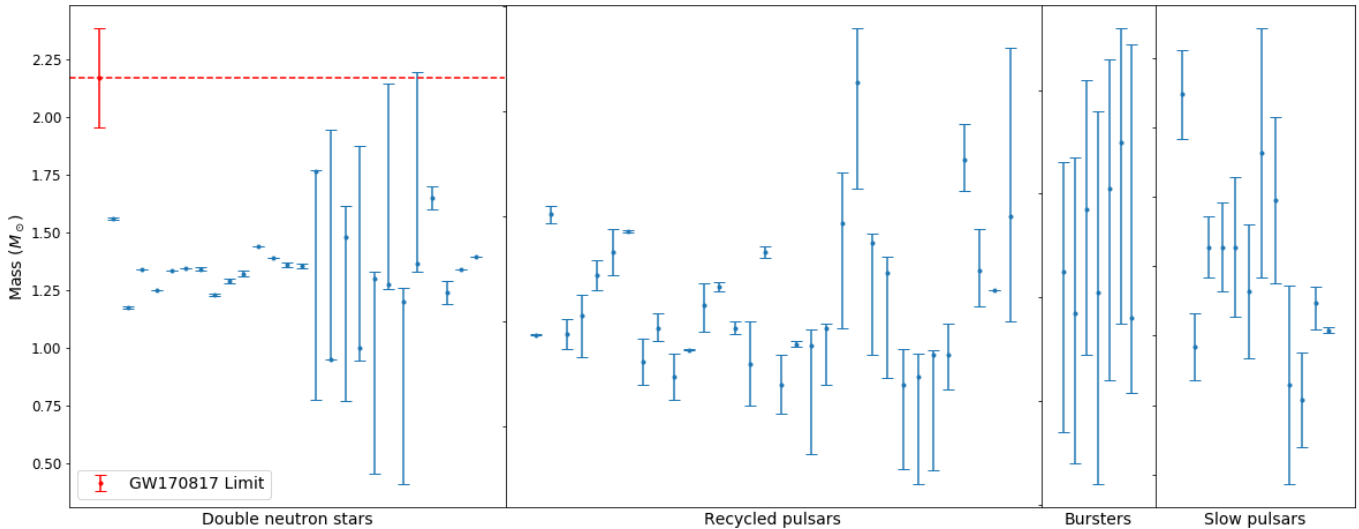
Figure 3. Inferred neutron star masses for source type using relativistic pulsar timing and Doppler spectroscopy. The upper mass limit obtained from the DNS GW170817 is shown in red (Margalit & Metzger 2017). Error bars indicate a 90% confidence interval.

narrowly peaked, symmetrical distribution for the mass likelihood of these pulsars. In cases where only one of the PK parameters is known, the likelihood function is expected to be highly asymmetric and more broadly peaked than for the two-PK-parameter DNS distribution.

3.2. *Doppler Spectroscopy*

Another way to measure the mass of a neutron star is through atomic spectral lines in the X-ray regime. For this method to be effective, the observed neutron star must have heavy metals in its atmosphere and a high enough temperature to emit significant thermal radiation. These features are characteristic of young pulsars, which have the required temperatures and frequently a high enough heavy metal fraction, and bursters, which renew their heavy metals through accretion and emit thermal radiation in large bursts due to shell burning.

The atomic lines in the spectra of these neutron stars are subject to many relativistic effects, such as Doppler boosting, strong self-lensing, frame-dragging, and differential gravitational redshift (Ozel & Psaltis 2003). It is possible to infer the mass-radius ratio of a neutron star from the gravitational redshift, with a correction for the asymmetries caused by a non-spherical rotator. Relativistic Doppler boosting causes the spectral lines to be doubly peaked, with the peak separation depending on the neutron star radius (Ozel & Psaltis 2003). From these effects, both the mass and the radius can be inferred for a neutron star of known spin frequency (Ozel & Psaltis 2003).

Detecting atomic lines in the spectrum of a neutron star is very difficult due to heavy rotational broadening, and the asymmetries in the spectral lines introduce large systematic uncertainties into calculation. As a result, this method of measurement remains too uncertain to effectively rule out most EoS models on its own (Ozel & Psaltis 2003). However, these masses are combined with the post-Keplerian mass measurements in our MCMC algorithm to improve our estimate of the overall distribution.

4. RESULTS

4.1. *Neutron Star Mass Distribution*

Although there have been on the order of 10^3 pulsars observed, only 10% are in binary systems (Abdo et al. 2013). Therefore, the current techniques relying on extracting mass information from orbital motion of the neutron star obtain a fairly small subset of the entire population. Despite this, precise Neutron Star (NS) mass measurements have been made using a variety of sources: Double Neutron Stars (DNS), Recycled Pulsars (RP), Bursters, and Slow Pulsars (SP). We add some newly discovered pulsars to the sample already included in Ozel & Freire (2016) — J1811+2405 Ng et al. (2020), J2302+4442 Kirichenko et al. (2018), J2215+5135 Linares et al. (2018), J1913+1102 Ferdman & Collaboration (2017), J1411+2551 Martinez et al. (2017), J1757+1854 Cameron et al. (2018), J0030+0451 Riley et al. (2019), J1301+0833 Romani et al. (2016) — and plot the masses in Figure 3 by their respective NS categorizations. We include the upper mass limit inferred from the GW170817 merger for reference. We
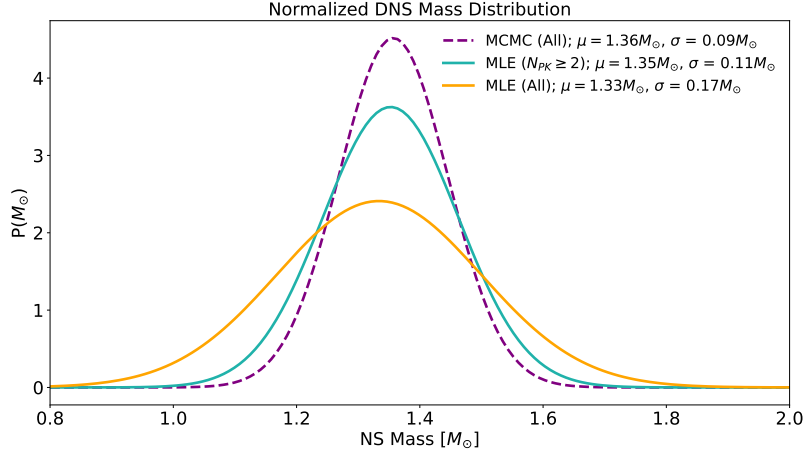
Figure 4. Normalized DNS mass distributions obtained using different statistical methods. Solid lines represent the distributions using the MLE approach while the dotted purple line represents our results for an MCMC Bayesian approach. N_{PK} refers to the number of determined post-keplerian parameters.

obtain constraints on the NS EoS using two statistical approaches: a simple MLE (Maximum Likelihood Estimation) method, and a Bayesian MCMC method adapted from (Kiziltan et al. 2010).

MLE

In order for our simple MLE approach to work, we assume that the mass distributions for each NS subtype are Gaussian, although it is yet to be determined whether this is truly the case. We also assume that the errors are small compared to the mass values, which is not true in all cases, although this does not change our results as much as one might think. There were 14 DNS observations where at least two PK parameters were determined (see Section 3.1), and these had smaller errors than those where only one was determined. We compare the inferred distribution of this subset of mass measurements to that of the full range of masses shown in the left-hand section of Figure 5 and observe a 36% improvement on the DNS mass constraint. Our values for $\mu \pm \sigma$ are $1.35 \pm 0.11 M_\odot$ and $1.33 \pm 0.17 M_\odot$ for the $N_{pk} \geq 2$ and the unfiltered DNS distributions, respectively. We repeat the MLE method for the RPs and obtain a a mean value of $1.66 M_\odot$ and a standard deviation of $0.25 M_\odot$.

We plot the normalized mass distributions for both the DNS and RPs in Figure 5. We define the least upper mass limit (lower limit on M_{max}) as the upper 2σ cutoff for both DNS and RPs. Based on our MLE approach, this cutoff corresponds to the values $M_{max} \geq 1.57 M_\odot$ and $M_{max} \geq 2.16 M_\odot$ for DNS and RP, respectively. This provides evidence for multi-modality in the overall NS distribution, with different peaks corresponding to different classes of Neutron Stars. The bimodal structure we find can be explained by a difference in composition and environment between the two classes, which likely results from a difference in formation histories (Kiziltan et al. 2010). As expected, the DNS distribution is narrower and taller compared to RPs, since precise DNS measurements are constrained to a tighter mass range. We note that the sample size for both NS categories is small, with $N_{DNS} = 14$ and $N_{RP} = 13$ for measurements with $\sigma_M \leq 0.1 M_\odot$, which somewhat invalidates an MLE approach in this case. However, as we will see in the next section, approximate results can still be obtained from this method, and future precise mass measurements will lend this approach more weight.

MCMC

To apply a more sophisticated approach to finding the NS mass distribution, we use the Bayesian statistical method described in Kiziltan et al. (2010). Assuming a Gaussian distribution of pulsars, the authors use the Metropolis-Hastings MCMC (Hastings 1970) algorithm to obtain the mean mass for their samples of DNS and NS-WD system measurements. A similar algorithm is used in Ozel & Freire (2016) and other papers on the NS mass distribution.

We use the same assumption here as in our MLE approach — that the NS distributions are Gaussian — but this time we quantify the mass errors, approximating them also as Gaussian distributions, and area able to specify our prior beliefs about μ and σ (see Appendix A). For the measurements with non-symmetric errors, we take the larger of the two error values to be 1σ. For a more thorough treatment of this problem, we would fit a more accurate probability distribution to the error values. but that is beyond the scope of this paper.
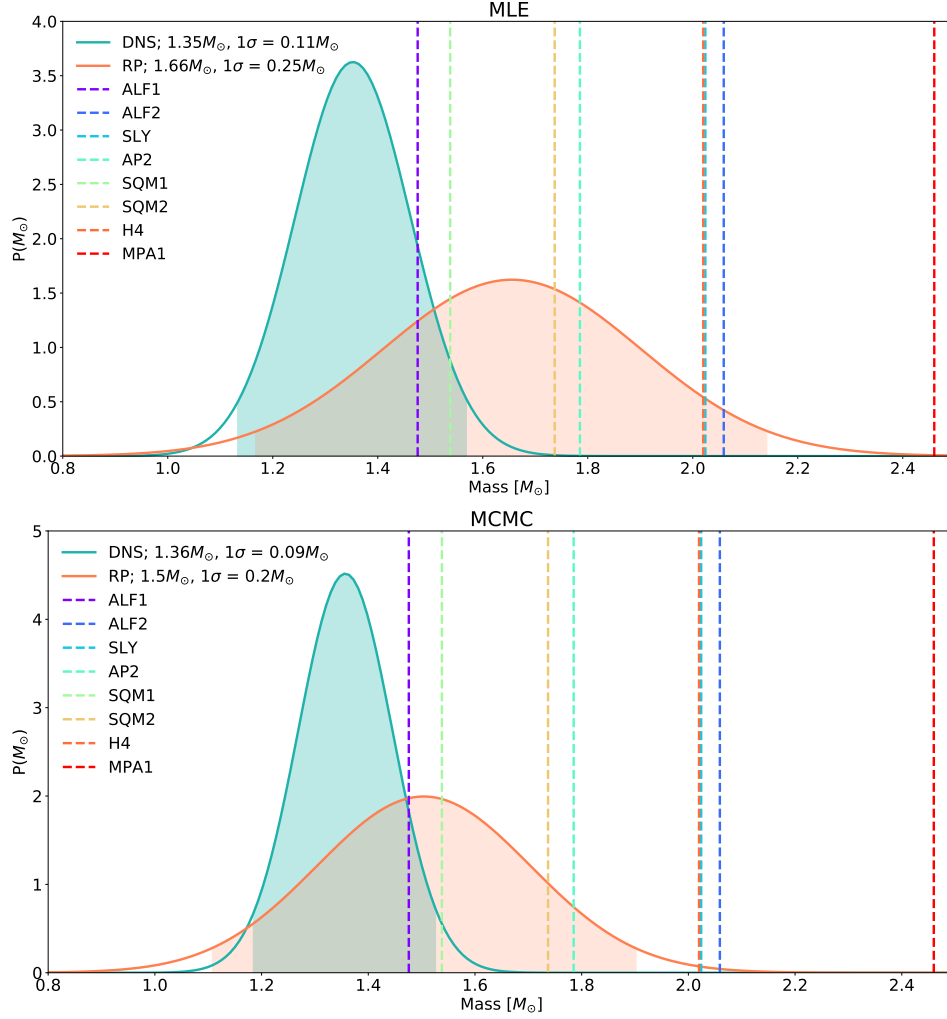
Figure 5. Bimodality of the DNS and RP mass distribution for MLE (top) and MCMC (bottom) algorithms. Shaded regions indicate 2σ confidence intervals. Dotted vertical lines represent the maximum predicted NS masses for our chosen EoS models.

NS type	M_{mean} ($M_\odot$)	σ^2 ($M_\odot$)	Least UL ($M_\odot$)
All	1.458 ± 0.025	0.037 ± 0.008	1.843 ± 0.049
DNS	1.357 ± 0.019	0.008 ± 0.003	1.536 ± 0.034
RPs	1.504 ± 0.036	0.040 ± 0.014	1.906 ± 0.076
Bursters	1.439 ± 0.047	0.002 ± 0.001	1.539 ± 0.055
SPs	1.394 ± 0.037	0.007 ± 0.005	1.556 ± 0.077

Table 2. MCMC results for the NS mass distribution. The lower limit on the maximum mass (Least Upper Limit) for each distribution is calculated in the farthest right column.

A detailed description of our approach can be found in Appendix A.

The main difference between this method and MLE are in the handling of errors and the quantification of uncertainty. MCMC methods model the posterior distribution of the data and are able to tell us the uncertainty of each estimated parameter. Prior beliefs can also be incorporated, making these algorithms well-suited for problems with uncertain or small sample sizes, such as this one. MLE, on the other hand, gives no estimates of the uncertainty of its results, and these results can sometimes be heavily influenced by outliers or uncertain data. In our simple MLE approach, we have also largely ignored the mass errors, which decreases the overall accuracy.

We find that the distribution obtained with MCMC is tighter than that obtained with MLE, even with the N_{pk} filters applied. This is likely due to the more accurate handling of individual measurement errors in the MCMC algorithm, as well as its increased performance on small datasets. The results of this method are summarized in Table 2. We can see that, though the MLE approach is less robust, it still gives approximate values for the DNS and RP masses, about $0.1M_\odot$ off in the latter case. We compare the MCMC results to those of our MLE analysis in Figures 4, 5, and 6, with the the
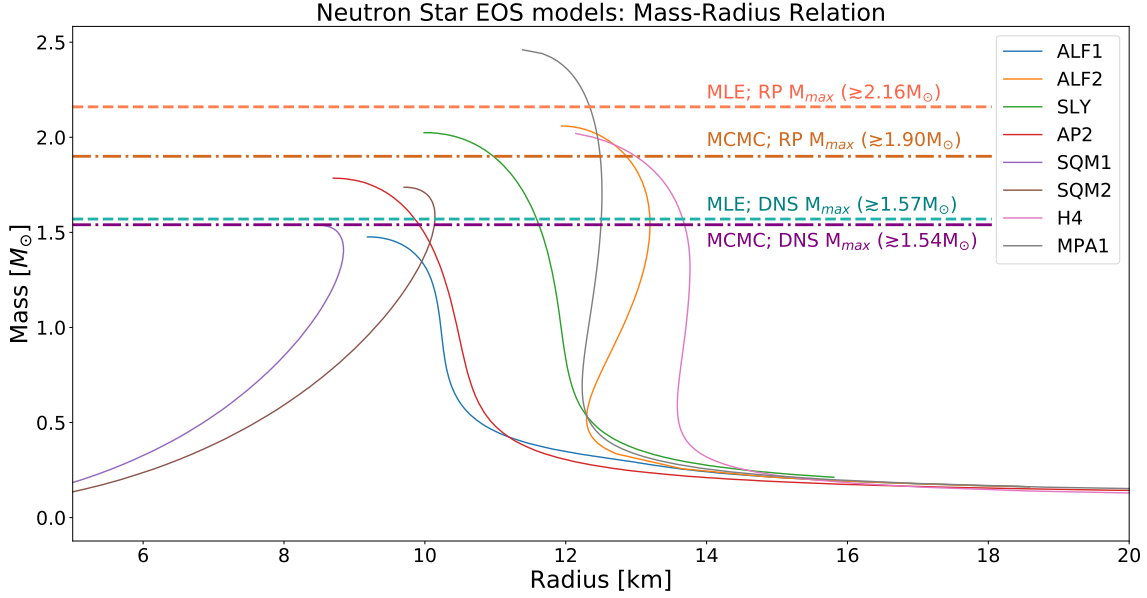
Figure 6. Mass-Radius relation for eight EoS models. The horizontal lines represent the least upper mass limits inferred from our MLE (dashed) and MCMC (dot-dashed) calculations.

maximum mass values of our eight EoS models included for reference.

4.2. *Constraints on the Equation of State*

Some EoS models can be ruled out using the observable NS parameters that we have found in previous sections. To show this, we use the collection of models described in Table 1 (ALF1/ALF2, SLy, AP2, SQM1/SQM2, H4, MPA1 (Alford et al. 2005; Douchin & Haensel 2001; Akmal et al. 1998; Prakash et al. 1995; Lackey et al. 2006; Müther et al. 1987)). In Figure 6, we plot the mass-radius relation of each EoS model, along with the observationally determined mass limits from our MLE and MCMC analyses. It is clear that the observations favor certain models: the lines shown for MLE and MCMC refer to the lower bounds on the high-mass cutoff of each distribution. Any model with a high-mass cutoff lower than these bounds can therefore be effectively ruled out.

The DNS measurements using MLE rule out the ALF1 and SQM1 models, which are the two softest EoS in our sample. However, DNS measurements using MCMC only rule out the ALF1 model. Our RP measurements using MLE rule out all of the models except for MPA1, which describes the stiffest equation of state in our sample. RP mass measurements using MCMC rule out fewer models: ALF1, SQM1, SQM2, and AP2. The two approaches have key differences, as the MCMC method is able to rule out fewer models in each case compared to

MLE due to the fact that it predicts a smaller limit on the maximum NS mass.

5. DISCUSSION

Although advancements have been made in the study of the Neutron Star mass distribution and equation of state, there is still much to be done before these are fully understood. New observational techniques could soon lead to advancements in the field, but the amount of mass and radius data available is lacking. In this paper, we combine mass measurements from several sources in order to verify existing research, and we compare two different statistical methods in our analysis. We confirm current measurements of the mean mass for different NS populations and are able to tighten the σ bounds as compared to previous analyses (Kiziltan et al. 2010). We find that it is important to use more advanced inference methods, such as MCMC, in data processing, as there is still too small a sample size to accurately make predictions with MLE. Finally, we show in our analysis that DNS mass limits tend to favor softer equation of state models, while RP mass limits tend to favor the stiffest ones. Using our collection of EoS models, we can infer that the DNS distribution may be populated by so-called hybrid stars (nuclear+quark matter), while RPs may have EoS models comprised mostly of nucleons. However, note that these results are somewhat dependent on the statistical treatment of the masses and

uncertainties, and may have different bounds under different approaches.

FUTURE WORK

The lower bound on M_{max} for the NS-NS (DNS) merger GW170817 is $\gtrsim 2.2 M_\odot$, which favors a stiffer EoS (Margalit & Metzger 2017). This result appears to contradict the mass distribution inferred from relativistic timing and Doppler spectroscopy methods. However, as the sample size of NS-NS gravitational-wave events is very small, more data is needed to confirm this discrepancy. Upgrades to the LIGO-Virgo gravitational wave detectors promise higher NS-NS merger rates, providing an opportunity to better constrain the NS mass distribution.

Due to the fact that there are very few simultaneous mass and radius measurements for neutron stars at the time of this paper, we choose to focus solely on the mass distribution in our analysis. In future work, we aim to incorporate radius measurements, which will place tighter constraints the on the true mass-radius relation and, therefore, the EoS. In addition, the interaction of matter at supra-nuclear densities is poorly understood at this time. In the next decade, improvements in nuclear physics may provide more robust models describing these supra-nuclear densities, which would contribute immensely to future studies of Neutron Star equations of state.

REFERENCES

Abbott, B., Abbott, R., Abbott, T., et al. 2017, Physical Review Letters, 119, 161101, doi: 10.1103/PhysRevLett.119.161101

Abdo, A. A., Ajello, M., Allafort, A., et al. 2013, The Astrophysical Journal Supplement Series, 208, 17, doi: 10.1088/0067-0049/208/2/17

Akmal, A., Pandharipande, V. R., & Ravenhall, D. G. 1998, Physical Review C, 58, 1804, doi: 10.1103/PhysRevC.58.1804

Alford, M., Braby, M., Paris, M., & Reddy, S. 2005, The Astrophysical Journal, 629, 969, doi: 10.1086/430902

Antoniadis, J., Freire, P. C. C., Wex, N., et al. 2013, Science, 340, 448, doi: 10.1126/science.1233232

Belczynski, K., Wiktorowicz, G., Fryer, C., Holz, D., & Kalogera, V. 2012, The Astrophysical Journal, 757, 91, doi: 10.1088/0004-637X/757/1/91

Cameron, A. D., Champion, D. J., Kramer, M., et al. 2018, Monthly Notices of the Royal Astronomical Society: Letters, 475, L57, doi: 10.1093/mnrasl/sly003

Desvignes, G., Caballero, R. N., Lentati, L., et al. 2016, Monthly Notices of the Royal Astronomical Society, 458, 3341, doi: 10.1093/mnras/stw483

Douchin, F., & Haensel, P. 2001, Astronomy & Astrophysics, 380, 151, doi: 10.1051/0004-6361:20011402

Ferdman, R. D., & Collaboration, t. P. 2017, Proceedings of the International Astronomical Union, 13, 146, doi: 10.1017/S1743921317009139

Hastings, W. K. 1970, Biometrika, 57, 97, doi: 10.1093/biomet/57.1.97

Hessels, J. W. T., Ransom, S. M., Stairs, I. H., et al. 2006, Science, 311, 1901, doi: 10.1126/science.1123430

Hulse, R. A., & Taylor, J. H. 1975, The Astrophysical Journal Letters, 195, L51, doi: 10.1086/181708

Kalogera, V., & Baym, G. 1996, The Astrophysical Journal Letters, 470, L61, doi: 10.1086/310296

Kirichenko, A. Y., Zharikov, S. V., Zyuzin, D. A., et al. 2018, Monthly Notices of the Royal Astronomical Society, 480, 1950, doi: 10.1093/mnras/sty1978

Kiziltan, B., Kottas, A., & Thorsett, S. E. 2010, arXiv:1011.4291 [astro-ph, stat]. http://arxiv.org/abs/1011.4291

Lackey, B. D., Nayyar, M., & Owen, B. J. 2006, Physical Review D, 73, 024021, doi: 10.1103/PhysRevD.73.024021

Lattimer, J. M., & Prakash, M. 2001, The Astrophysical Journal, 550, 426, doi: 10.1086/319702

Leeuwen, J. v., Kasian, L., Stairs, I. H., et al. 2015, The Astrophysical Journal, 798, 118, doi: 10.1088/0004-637X/798/2/118

Linares, M., Shahbaz, T., & Casares, J. 2018, The Astrophysical Journal, 859, 54, doi: 10.3847/1538-4357/aabde6

Margalit, B., & Metzger, B. 2017, The Astrophysical Journal, 850, L19, doi: 10.3847/2041-8213/aa991c

Martinez, J. G., Stovall, K., Freire, P. C. C., et al. 2017, The Astrophysical Journal, 851, L29, doi: 10.3847/2041-8213/aa9d87

Müther, H., Prakash, M., & Ainsworth, T. L. 1987, Physics Letters B, 199, 469, doi: 10.1016/0370-2693(87)91611-X

Ng, C., Guillemot, L., Freire, P. C. C., et al. 2020, Monthly Notices of the Royal Astronomical Society, 493, 1261, doi: 10.1093/mnras/staa337

Ozel, F., & Freire, P. 2016, doi: 10.1146/annurev-astro-081915-023322

Ozel, F., & Psaltis, D. 2003, The Astrophysical Journal, 582, L31, doi: 10.1086/346197

Prakash, M., Cooke, J. R., & Lattimer, J. M. 1995, Physical Review D, 52, 661, doi: 10.1103/PhysRevD.52.661

Raithel, C. A., Özel, F., & Psaltis, D. 2017, The Astrophysical Journal, 844, 156, doi: 10.3847/1538-4357/aa7a5a

Reardon, D. J., Hobbs, G., Coles, W., et al. 2016, Monthly Notices of the Royal Astronomical Society, 455, 1751, doi: 10.1093/mnras/stv2395

Rhoades, C. E., & Ruffini, R. 1974, Physical Review Letters, 32, 324, doi: 10.1103/PhysRevLett.32.324

Riley, T. E., Watts, A. L., Bogdanov, S., et al. 2019, The Astrophysical Journal, 887, L21, doi: 10.3847/2041-8213/ab481c

Romani, R. W., Graham, M. L., Filippenko, A. V., & Zheng, W. 2016, The Astrophysical Journal, 833, 138, doi: 10.3847/1538-4357/833/2/138

Taylor, J. H. 1993, Classical and Quantum Gravity, 10, S167, doi: 10.1088/0264-9381/10/S/017

APPENDIX

A. BAYESIAN MCMC MODEL

Here, we summarize the statistical method adopted from Kiziltan et al. (2010). This method attempts to model the posterior of the measured NS data through a randomized Markov-Chain-Monte-Carlo (MCMC) method. It is particularly applicable in problems in which there is a small amount of data available, as is the case here (26 DNSs, 32 RPs, 7 Bursters, 12 SPs), compared to the MLE method discussed previously, which relies on a large sample size for uncertainty estimates. When applied correctly, MCMC is able to accurately the uncertainty of its own results even when the sample size is small. We model the neutron star distribution as a Gaussian with some mean and standard deviation. The likelihood of this distribution is then described by:

$$\mathcal{L}(\mu, \sigma^2 | \text{data}) = \frac{P(\text{data}|\mu, \sigma^2)P(\mu)P(\sigma^2)}{P(\text{data})} \tag{A1}$$

$$\propto \mathcal{L}(\text{data}|\mu, \sigma^2)\pi(\mu)\pi(\sigma^2) \tag{A2}$$

$$\mathcal{L}(\text{data}|\mu, \sigma^2) = \prod_i^N [2\pi(\sigma^2 + S_i^2)]^{-1/2} e^{-\frac{(m_i - \mu)}{2(\sigma^2 + S_i^2)}} \tag{A3}$$

$$\tag{A4}$$

Where m_i and S_i are the values for the mass and mass error of measurement i, respectively. The prior distributions for the parameters μ and σ, also adopted from Kiziltan et al. (2010), are modeled as Normal and Inverse Gamma distributions, respectively. These priors are tuned with the hyperparameters a, b, c, and d, as shown below:

$$\pi(\mu) = N(a, b^2) = (2\pi b^2)^{-1/2} \exp\left[-\frac{(\mu - a)^2}{2b^2}\right] \tag{A5}$$

$$\pi(\sigma^2) = \Gamma^{-1}(c, d) = \frac{d^c e^{-d/\sigma^2}}{\Gamma(c)\sigma^{2(c+1)}} \tag{A6}$$

Since a more rigorous search for the best hyperparameters is beyond the scope of this paper, we use the best results from Kiziltan et al. (2010), which are as follows: $a = 1.4$, $b = 0.05$, $c = 5$, $d = 0.01$. As much of our data comes from this paper, the best values for our data should not vary significantly from these. The full expression for the posterior distribution (in log form) is shown below:

$$\log(\mathcal{L}(\mu, \sigma^2|\text{data})) = -\frac{1}{2}\sum_i^N \frac{(m_i - \mu)^2}{\sigma^2 + S_i^2} + \log(\sigma^2 + S_i^2) + \log(\pi(\mu)) + \log(\pi(\sigma)) \tag{A7}$$

The algorithm generates values of μ and σ from their prior distributions, and compares the posteriors of the results using equation A7. If a μ, σ combination is more likely than the current one, the step will be accepted, and if not it will be rejected with some probability related to the likelihood. If the data is modeled correctly, the algorithm will converge to the true posterior distribution. Sample convergence plots for our algorithm are shown in Figure 7. The lack of any clear features in the μ and σ^2 samples from each Markov chain is strong evidence that the algorithm has converged.
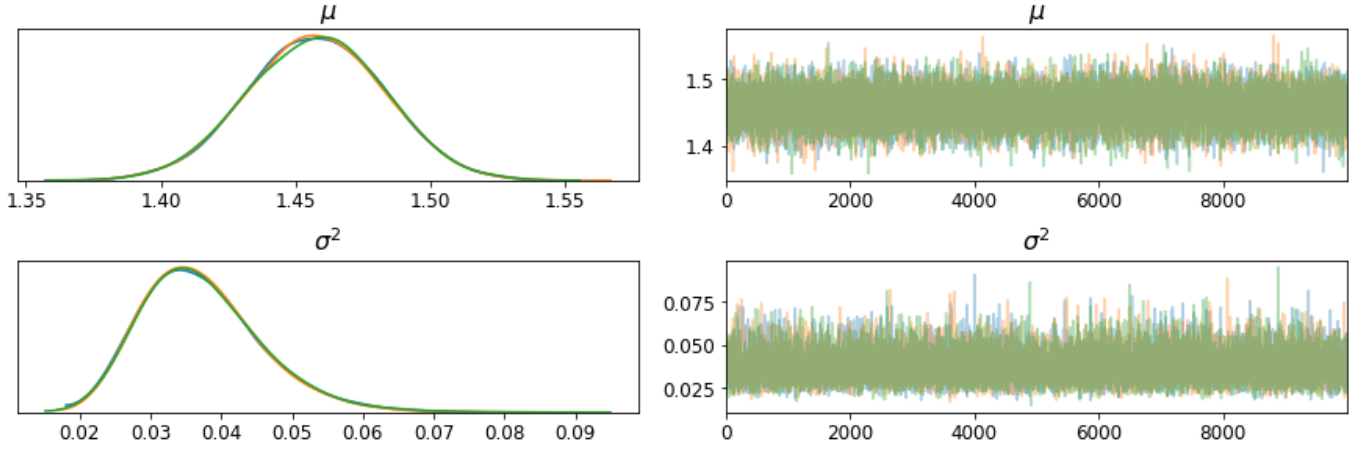
Figure 7. Convergence of the MH-MCMC algorithm with three Markov chains and 10,000 steps, run on the full set of NS masses. The left plots shows a histogram of each parameter while the right plots show individual samples from the Markov chains.